Aluminum-induced colloidal destabilization of iron-organic matter nanoaggregates

Anthony Beauvois, Delphine Vantelon, Jacques Jestin, Aurélien Dupont, Valérie Briois, Erwan Paineau, Thomas Bizien, Alice Pradel, Mélanie Davranche

Journal Pre-proofs

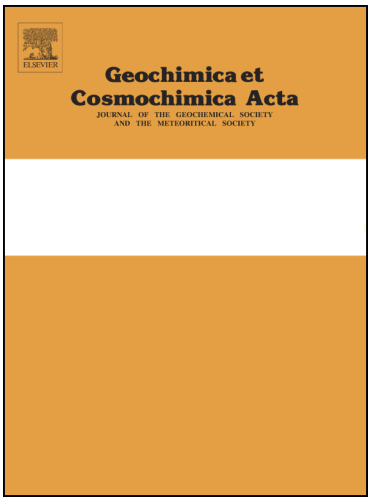

Aluminum-induced colloidal destabilization of iron-organic matter nanoaggregates

Anthony Beauvois, Delphine Vantelon, Jacques Jestin, Aurélien Dupont, Valérie Briois, Erwan Paineau, Thomas Bizien, Alice Pradel, Mélanie Davranche

PII: S0016-7037(23)00006-6
DOI: https://doi.org/10.1016/j.gca.2023.01.005
Reference: GCA 12926

To appear in: *Geochimica et Cosmochimica Acta*

Received Date: 11 March 2022
Revised Date: 3 January 2023
Accepted Date: 4 January 2023

Please cite this article as: Beauvois, A., Vantelon, D., Jestin, J., Dupont, A., Briois, V., Paineau, E., Bizien, T., Pradel, A., Davranche, M., Aluminum-induced colloidal destabilization of iron-organic matter nanoaggregates, *Geochimica et Cosmochimica Acta* (2023), doi: https://doi.org/10.1016/j.gca.2023.01.005

Aluminum-induced colloidal destabilization of iron-organic matter nanoaggregates

Anthony Beauvois[a,b,c*], Delphine Vantelon[b], Jacques Jestin[c ‡], Aurélien Dupont[d], Valérie Briois[b], Erwan Paineau[e], Thomas Bizien[b], Alice Pradel[a], and Mélanie Davranche[a]

[a]*Univ. Rennes, CNRS, Géosciences Rennes - UMR 6118, F-35000 Rennes, France*

[b]*Synchrotron SOLEIL, L'Orme des Merisiers, Départementale 128, 91190 Saint-Aubin*

[c]*Laboratoire Léon Brillouin, CEA Saclay, 91191 Gif-sur-Yvette Cedex*

[d]*CNRS, Inserm, BIOSIT – UMS 3480, Univ Rennes, US_S 018, F-35000 Rennes, France*

[e]*Université Paris-Saclay, CNRS, Laboratoire de Physique des Solides, 91405 Orsay, France*

[*]*Corresponding author: anthony.beauvois@synchrotron-soleil.fr*

[‡] *Present address: Institut Laue-Langevin, 6 rue Jules Horowitz, 38000 Grenoble, France.*

Abstract

The structural organization of heterogeneous and multiphase natural aggregates depends on the biophysicochemical conditions prevailing in the environment, with major ions playing a crucial role. In this study, the impact of aluminum (Al) on iron-organic matter (Fe-OM) aggregates was investigated since Al can interact with OM and can be incorporated in Fe-oxyhydroxides or adsorbed on their surface. Mimetic environmental Fe-OM-Al aggregates were synthesized at various [Fe] and [Al] with a constant [OM]. At low [Al+Fe], Fe-OM-Al aggregates exhibit a colloidal behavior. Within the aggregates, Fe is present as Fe(III)-oligomers and ferrihydrite-like nanoparticles whereas Al forms monomers, oligomers and small polymers, all bound to OM. The Al and Fe phases interacted with each other. At high [Fe+Al], the Fe(III)-oligomers and Al monomers/oligomers polymerized which increases the size and quantity of the ferrihydrite-like nanoparticles and Al polymers and then branched out the OM, resulting in a large settling network. The effect of Al on the Fe-OM aggregates structure could also have an impact on the fate of pollutants. The occurrence of Al amorphous hydroxides and the increase in ferrihydrite-like nanoparticles lead to a higher availability of surface reactive sites and subsequently to an increase in the sorption capacity of the Fe-OM aggregates for pollutants that exhibit a greater affinity for minerals than for organics.

Keywords

Ferrihydrite, humic acid, aluminum, XAS, SAXS

1. Introduction

It is now widely recognized that heterogeneous colloids and nano-aggregates control the biogeochemical cycle of many contaminants (Wigginton et al., 2007; Pédrot et al., 2008; Stolpe et al., 2013; ThomasArrigo et al., 2014; Guénet et al., 2016). Among these colloids and aggregates, iron-organic matter (Fe-OM) nanoaggregates in particular are ubiquitous in many environmental systems such as wetlands, peatlands or permafrost where they are formed mainly as result of soil alteration and erosion, and oxidation-reduction cycles due to alternating periods of waterlogging and desaturation (Pokrovsky and Schott, 2002; Pokrovsky et al., 2005; ThomasArrigo et al., 2014; Guénet et al., 2016; Hirst et al., 2017; Ratié et al., 2019; Lotfi-Kalahroodi et al., 2019). As a result, Fe-OM nanoaggregates have been intensively studied over the last decade (Pokrovsky and Schott, 2002; Karlsson et al., 2008; Pédrot et al., 2008, 2011; Stolpe et al., 2013; ThomasArrigo et al., 2014; Guénet et al., 2017; Beauvois et al., 2020, 2021).

The ability for Fe-OM nanoaggregates to control the dynamics of metal and metalloid pollutants, particularly through adsorption processes, strongly depends on the structure and notably the physico-chemical interaction between the Fe phases and the OM macromolecules and colloids (Ritter et al., 2006; Mikutta and Kretzschmar, 2011; Guénet et al., 2017). The structure of Fe-OM aggregates may strongly vary with the prevailing physicochemical conditions, such as the pH or the presence of major ions. Recently, Beauvois et al. (2020) demonstrated that the overall structure of Fe-OM aggregates is strongly influenced by the presence of Ca which drives a structural transition from Fe-OM colloidal aggregates to a Ca-branched micrometric network, which decreases the mobility of Fe-OM aggregates in the environment. By acting as a Fe competitor, Ca indirectly triggers the formation of ferrihydrite-like nanoparticles (Fh-like Nps) rather than Fe(III)-oligomers. The major consequence of this includes the increase of Fe-OM aggregates sorption capacities for contaminants with a higher

affinity for mineral phases rather than for organic phases, such as arsenic (As) (Beauvois et al., 2020, 2021).

However, in environmental systems, Ca is not the only major ion. Among the other elements present, aluminum (Al) is of peculiar interest given its high concentration (Klöppel et al., 1997; Dia et al., 2000; Tipping, 2005; Pokrovsky et al., 2005; Ščančar and Milačič, 2006) and the control that it might exert on the structure of Fe-OM aggregates. Aluminum is known to have high affinity for natural OM (Lippold et al., 2005; Tipping, 2005; Marsac et al., 2012; Adusei-Gyamfi et al., 2019). Several studies have demonstrated that the interaction between Al and OM has an impact on Al speciation (Hu et al., 2008; Hay and Myneni, 2010; Xu et al., 2010; Hagvall et al., 2015). Organic matter limits the crystallinity of the formed Al-hydroxides and even prevents Al polymerization at high OM/Al ratios (Hay and Myneni, 2010; Hagvall et al., 2015). Moreover, Hagvall et al. (2015) provided evidence of the formation of mononuclear Al chelate with OM via its carboxylic sites. Aluminum is also known to strongly interact with Fe since Al can be incorporated in the structure of Fe (hydr)oxides such as in lepidocrocite for an Al/Fe molar ratio up to 0.1-0.2 (Kim et al., 2015; Liao et al., 2020) and goethite or ferrihydrite for an Al/Fe molar ratio up to 0.3-0.4 (Hazemann et al., 1991; Hansel et al., 2011; Cismasu et al., 2012; Adra et al., 2013). In their study, Adra et al. (2016) demonstrated that the more Al incorporated the Fh structure, the more As(V) adsorption increased while that of As(III) decreased. The occurrence of Al therefore may strongly impact the structures and behavior of Fe-OM aggregates forming natural mixed Fe-OM-Al aggregates (Pokrovsky et al., 2005). Nierop et al. (2002) observed that OM binds both Fe and Al. Furthermore, they reported that at a low (Fe+Al)/organic carbon (OC) ratio, Al controlled the precipitation of the aggregates since, in their study, the Al concentration was higher than the Fe(III) concentrations.

To determine the impact of Al on the adsorption capacity of Fe-OM aggregates and on their ability to transport metal(loid)s pollutant, a crucial first step, but currently still missing, is

to perform a complete multi-scale description of the structural arrangement of these aggregates as a function of the presence of Al. The objective of the present study is therefore to study in depth the impact of Al on the organization of mineral and organic phases within the aggregates, and the interaction between the phases. This will be achieved through a thorough characterization of (i) the speciation of Al, (ii) the modes of interaction with Fe and OM phases, if any, and (iii) the resulting changes in the structural organization of Fe-OM-Al aggregates, having dramatic impact on metal(loid)s pollutant behavior in natural systems. For this purpose, mimetic environmental Fe-OM-Al aggregates were synthesized at various Fe/OC and Al/Fe molar ratios. Aluminum-substituted Fh and Al-OM associations at various Al/OM molar ratios were also prepared before being thoroughly characterized in order to be used as references. The structural organization of the Fe-OM-Al nanoaggregates, from the atomic to micrometric scale, was investigated using a combination of complementary techniques. First, Al interactions with the Fe phases and OM were probed by X-ray absorption near edge structure (XANES) at the Al K-edge. To obtain an overview of the impact of Al on the structural organization of Fe, Fe speciation within the Fe-Al-OM aggregates was studied by performing a Fe K-edge extended X-ray absorption fine structure (EXAFS) analysis. The arrangement of Fh-like nanoparticles within the aggregates was investigated by small-angle X-ray scattering (SAXS) experiments. Finally, the overall organization of the aggregates was observed with cryo-transmission electron microscopy (cryo-TEM).

2. Materials and methods

2.1. Sample synthesis and elemental composition

Synthesis of Fe-OM-Al aggregates

Fe-OM-Al aggregates were synthesized following the procedure described by Beauvois et al. (2020). Four Fe^{2+}-Al^{3+} stock solutions were prepared at $[Fe^{2+}] = 1.8\times10^{-2}$ mol L^{-1} and Al/Fe molar ratios = 0, 0.1, 0.5, 1.0 using $FeCl_2.4H_2O$ and $AlCl_3$ (Sigma Aldrich). Fe(II) as

source of iron was chosen to reproduce the oxidation step of oxidation-reduction cycles occurring in natural systems. An OM stock solution was prepared at 1.00×10^{-1} mol L^{-1} with Leonardite humic acid (LHA) (International Humic Substances Society). The LHA, with the elemental composition C = 63.81%, O = 31.27%, H = 3.70% and N = 1.23% (as a mass fraction), was chosen regarding its representativeness of the natural OM in wetlands systems (Thurman, 1985). To synthesize the Fe-OM-Al aggregates, an *ad hoc* volume Fe^{2+}(-Al^{3+}) stock solution was progressively added to the OM suspension to reach [OC] = 60.5 mmol L^{-1} and Fe/OC molar ratios = 0.02, 0.05 and 0.08 for each Al/Fe ratios. The addition was performed at 0.05 mL min^{-1} in 5×10^{-3} mol L^{-1} of NaCl using an automated titrator (Titrino 794, Metrohm) under ambient air conditions. During the procedure, the pH was monitored at 6.5 ± 0.04 with a 0.1 mol L^{-1} NaOH solution using a second titrator in a set pH mode. At the end of the addition, the pH was continuously monitored during 24h for stabilization.

Finally, Fe-OM-Al aggregates were synthesized at pH = 6.5, at three Fe/OC (0.02, 0.05 and 0.08) and four Al/Fe (0, 0.1, 0.5 and 1) molar ratios (Figure 1). These conditions were chosen in line with those reported for natural wetlands by Dia et al. (2000) with Fe/OC and Al/Fe molar ratios and pH ranging from 0.001 to 0.09, 0.1 to 1.5 and 5.9 to 7, respectively. In this work, samples were labelled Fe*x*-Al*y*, where *x* and *y* represent the Fe/OC and Al/Fe ratios, respectively (Table 1).

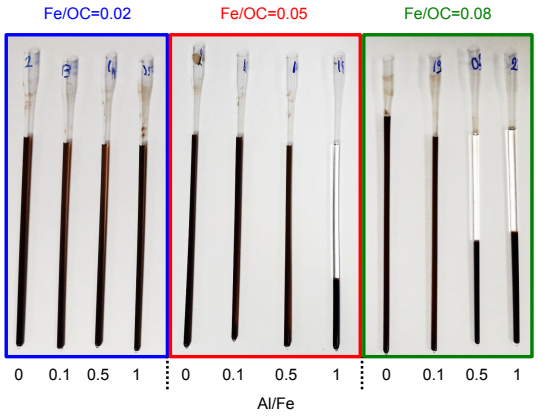

Figure 1 – Fe-OM-Al aggregates within capillaries for SAXS measurements after they were stored vertically for 2 months.

Synthesis of ferrihydrite, poorly crystalized Al hydroxide and Al substituted ferrihydrite

Ferrihydrite (Fh), poorly crystalized Al hydroxide (Al-hydrox) and Al-substituted ferrihydrite (Al-Fh) with an Al/Fe molar ratio = 0.4 were synthesized following the procedure described by Schwertmann and Cornell (2000). Stock solutions of Fe^{3+}, Al^{3+} and Fe^{3+}-Al^{3+} (with an Al/Fe molar ratio = 0.4) were prepared by dissolving $Fe(NO_3)_3.9H_2O$ and $Al(NO_3)_3.9H_2O$ (Sigma Aldrich). References were prepared by rapidly setting the pH of the corresponding stock solution to 7 (to ensure a monophasic formation) with a 1 mol L^{-1} KOH solution using a Mettler Toledo SevenEasy TM pH-meter, under continuous stirring (at 250 rpm). After 24h, the suspensions were centrifuged at 8872 g and washed three times with Milli-Q water. The precipitates were dried and shredded at room temperature.

Synthesis of Al-OM aggregates

The Al-OM aggregates were prepared by dissolving $AlCl_3$ (Sigma Aldrich) in a LHA suspension with [OC] = 60.5 mmol L^{-1} at three Al/OC molar ratios (0.0003, 0.002 and 0.086). The pH was adjusted to 6.5 using 0.1 mol L^{-1} HCl or NaOH solution and the suspensions were stirred 24h after which the pH was adjusted again if necessary. The Al/OC = 0.0003 ratio was calculated with the visual Minteq software to be the highest while avoiding Al precipitation. The ratios Al/OC = 0.002 and 0.086 were chosen as they corresponded to the Al/OC ratios within Fe0.02-Al1.0 and Fe0.08-Al1.0, respectively. The samples were labelled Al-OM*z* where *z* refers to the Al/OC molar ratio.

Chemical analysis of samples

The Fe and Al concentrations within the Fe-OM-Al aggregates were determined by the ICP-OES measurements performed on a PlasmaQuant PQ 9000 Elite instrument (Analytik Jena). Prior to the measurements, the OM was eliminated by digesting 0.25 mL of the sample with 14.6 mol L^{-1} HNO_3 using a Discover SP-D 80 microwave (CEM) operating at 300 W and 175°C for 5 min. The OC concentrations were measured using an organic carbon analyzer

(Shimadzu TOC-V CSH). The measured concentrations (Table S1) allowed to calculate the experimental molar ratio within the Fe-OM-Al aggregates (Table 1).

Table 1 – Overview of the sample and reference names with the corresponding Fe/OC, Al/Fe and Al/OC molar ratios. Exp: experimental. Theo: theoretical. n.d.: not determined. A '-' is reported when the ratio was not suitable.

	Sample name	Fe/OC (mol/mol)		Al/Fe (mol/mol)		Al/OC (mol/mol)	
		Exp	Theo	Exp	Theo	Exp	Theo
Fe-OM-Al aggregates	Fe0.02-Al0.0	0.02	0.02	0.08	0.0	0.002	0.000
	Fe0.02-Al0.1	0.03	0.02	0.17	0.1	0.004	0.002
	Fe0.02-Al0.5	0.02	0.02	0.68	0.5	0.016	0.011
	Fe0.02-Al1.0	0.03	0.02	1.06	1.0	0.027	0.021
	Fe0.05-Al0.0	0.05	0.05	0.03	0.0	0.002	0.000
	Fe0.05-Al0.1	0.07	0.05	0.11	0.1	0.008	0.005
	Fe0.05-Al0.5	0.06	0.05	0.50	0.5	0.028	0.027
	Fe0.05-Al1.0	0.06	0.05	0.96	1.0	0.057	0.054
	Fe0.08-Al0.0	0.08	0.08	0.02	0.0	0.002	0.000
	Fe0.08-Al0.1	0.09	0.08	0.09	0.1	0.008	0.005
	Fe0.08-Al0.5	0.09	0.08	0.47	0.5	0.042	0.043
	Fe0.08-Al1.0	0.10	0.08	0.94	1.0	0.094	0.086
References	Fh	-	-	-	-	-	-
	Al-hydrox	-	-	-	-	-	-
	Al-Fh	-	-	n.d.	0.4	-	-
	Al-OM0.0003	-	-	-	-	n.d.	0.0003
	Al-OM0.002	-	-	-	-	n.d.	0.002
	Al-OM0.086	-	-	-	-	n.d.	0.086

2.2. Structural characterizations

XAS data acquisition and analysis

The speciation of Al and Fe within Fe-OM-Al aggregates was investigated by X-ray absorption spectroscopy at the Al and Fe K-edge, respectively. The suspensions were freeze-dried (Freeze dryer Alpha 1-2 LD plus, Christ) before being conditioned prior to XAS analyses.

For the Al K-edge XANES measurements, the powders were crushed on an indium foil and fixed on a copper plate. Natural gibbsite (Vaucluse, France), Al-hydrox, Al-Fh and Al-OM aggregates were prepared following the same protocol as Fe-OM-Al aggregates and their Al K-

edge XANES were recorded to be used as reference. The spectra were recorded on the LUCIA beamline (Flank et al., 2006; Vantelon et al., 2016) at the SOLEIL synchrotron equipped with a KTP(011) double-crystal monochromator. Measurements were taken at room temperature, under primary vacuum (10^{-2} mbar) conditions, in fluorescence mode using a 60 mm² mono-element silicon drift diode detector (Bruker) and corrected for the detector dead time. The energy was calibrated by setting the first inflexion point at the Al K-edge of an Al foil at 1559 eV.

For the XAS measurements at the Fe K-edge, powders were mixed with cellulose and pressed into a 6 mm pellet. The same goes for Fh, which was used as reference. The measurements were performed on the ROCK beamline (Briois et al., 2016) at the SOLEIL synchrotron using a Si(111) channel-cut as monochromator. The spectra were recorded at room temperature in transmission mode using ionization chambers (Ohyo Koken) filled with N_2. A Fe foil located between the 2nd and 3rd ionization chamber was measured along with the samples to calibrate the energy by setting the first inflexion point of the XANES spectrum of the Fe foil to 7112 eV.

All of the XAS data were processed with the Athena software including the Autbk algorithm (Rbkg = 1, k-weight = 3) (Ravel and Newville, 2005). The spectra were normalized by fitting the pre-edge region with a linear function and the post-edge region with a quadratic polynomial function. The Fourier transforms (FT) of the k^3-weighted EXAFS spectra were calculated over a range of 2-12.5 $Å^{-1}$ using a Hanning apodization window (window parameter = 1). The EXAFS data were analyzed using a linear combination fit (LCF) available in the Athena software within the range 3-12.5 $Å^{-1}$; all of the component weights were forced to be positive. The references used were Fh, and two pure components extracted from the *in situ* synthesis of Fe-OM aggregates by Vantelon et al. (2019), i.e. Fe(III)-oligomers and small nanoparticles of Fh (small-Fh), all bound or embedded in a HA matrix. The best LCF fit was

determined for the minimum *n*-components for which the R-factor was better than 10% of the fit with *n+1* components. Without any constraints, the total LCF weight for each sample was between 0.95 and 1.05, it was therefore arbitrarily fixed to 1 to facilitate comparisons between each sample. The error on the weight of each component was set to the average error reported by the Athena software, i.e. 10%. The Al data were corrected for self-absorption based on the theoretical chemical formula of the mineral phases contained in the samples and by applying the procedure provided in the Athena software. For better clarity of the plots, the data were slightly smoothed using the iterative smoothing procedure of the Athena software, setting the number of iterations to 1. A natural gibbsite (from Vaucluse, France) was used as a reference for the processing of the Al K-edge experiments.

SAXS measurements

The organization of Fe(III) particles within Fe-OM-Al aggregates was probed with small-angle X-ray scattering. Prior to the measurements, an aliquot of Fe-OM-Al aggregates was introduced into 1.5 mm diameter borosilicate capillaries. The SAXS curves were recorded on the SWING beamline at the SOLEIL synchrotron. Two sample-to-detector distances (1 and 6 m) were used with a wavelength of 1.03 Å to reach a diffusion vector, q, range of 2.0×10^{-3}-0.7 $Å^{-1}$. It allows to probe objects which size varies from around 0.8 nm to 300 nm. The measurements were carried out on either the suspension or precipitate for the settled samples (Figure S1). A capillary filled with ultrapure water was also measured as reference.

In a first step, the contribution of the capillary and water to the SAXS signal was removed by subtracting the curve of the water to each curve of Fe-OM-Al aggregates. Then, the obtained curves were analyzed using the same cluster fractal model previously described in previous studies on Fe-OM aggregates (Guénet et al., 2017; Beauvois et al., 2020). This model is based on an-exponential-power law approximation (Beaucage, 1996). According to this

(eq. 1)

model, the scattered intensity I(q) of centrosymmetric nanoparticles dispersed in a continuous solvent is described by eq. 1:

$$I(q)=\varphi.V.\Delta\rho^2.P(q).S(q)$$

where φ is the volume fraction, V is the volume of the scattered entities, $\Delta\rho^2$ is the contrast term, and P(q) and S(q) are the form and the structure factor, respectively. The model was built considering that Fe is organized as spherical poly-dispersed primary beads (Fe-PB) aggregated into a Fe primary aggregate (Fe-PA). The Fe-PA are described by a form factor according to a finite number of Fe-PB and a fractal dimension, and can be aggregated as a Fe secondary aggregate (Fe-SA).

Cryo-TEM imaging

The overall structure of Fe-OM-Al aggregates was probed recording cryo-transmission electron microscopy images (cryo-TEM). The measurements were done on two samples with distinct macroscopic behavior: Fe0.08-Al0.1 (which did not settle, Figure 1) and Fe0.08-Al1.0 (which settled, Figure 1). One drop of each sample was deposited on a glow-discharged carbon coated copper grid. The grid was blotted and vitrified by rapid freezing in liquid ethane (-184°C) using a Leica EM GP immersion freezer. Grids were introduced in a single-axis cryo-holder (model 626, Gatan) and observed using a 200 kV electron microscope (Tecnai G2 T20 Sphera, FEI) equipped with a 4k x 4k CMOS camera (model TemCam-F416, TVIPS). Images were recorded under low electron doses using the camera in binning mode 1 and at a nominal magnification of ×50,000.

3. Results

3.1. Aluminum speciation within Fh

All of the Al K-edge XANES spectra exhibited a white line centered at ~ 1570 eV and were representative of Al in octahedral symmetry (Ildefonse et al., 1998; Cismasu et al., 2012; Hofmann et al., 2013) (Figure 2a). Except for Fe0.02-Al0.1, the XAS spectra of the related

samples containing Fe always exhibited a pre-edge at ~ 1562 eV (Figure 2b) which reveals the presence of Al-O-Fe bonds (Ducher et al., 2016). This pre-edge is weaker for the Fe-OM-Al aggregates than those observed for Al-Fh0.40 suggesting that only a fraction of Al interacts with Fe. The XANES spectra of the Al-OM and Fe-OM-Al samples were poorly structured compared to those of gibbsite and Al-hydrox. This observation suggests the absence of Al hydroxide precipitation and low Al polymerization in the presence of OM. This assumption is confirmed by the edge position expressed by the maximum of the first XANES derivate (Figure 2c). Hagvall et al. (2015) reported an energy shift to high values between gibbsite, Al-OM complexes and free Al(III), the latter was measured at pH = 1.9 which ensured dispersed Al^{3+} monomers surrounded by 6 O. In our data, the edge position of the Al XANES spectra shifted by ~ 2 eV between Al-hydrox and Al-OM0.0003. Considering the high affinity of Al for binding OM (Lippold et al., 2005; Tipping, 2005; Marsac et al., 2012) and given that the Al concentration in Al-OM0.0003 was selected to avoid Al precipitation, Al within Al-OM0.0003 can be considered as monomers bound to OM. With the increasing [Al] at pH = 6.5, the polymerization-condensation of Al was expected (Bi, 2004). Consequently, the edge position of Fe-OM-Al and Al-OM spectra continuously shifted to lower energy with the decreasing OC/Al ratio (Figure 2d and Table SI-3). Finally, the pre-edge occurrence as well as the edge position of the Al XANES spectra demonstrated that Al within Fe-OM-Al aggregates is organized as monomers bound to OM which polymerized with the increasing [Al], and partially interacted with the Fe phases.

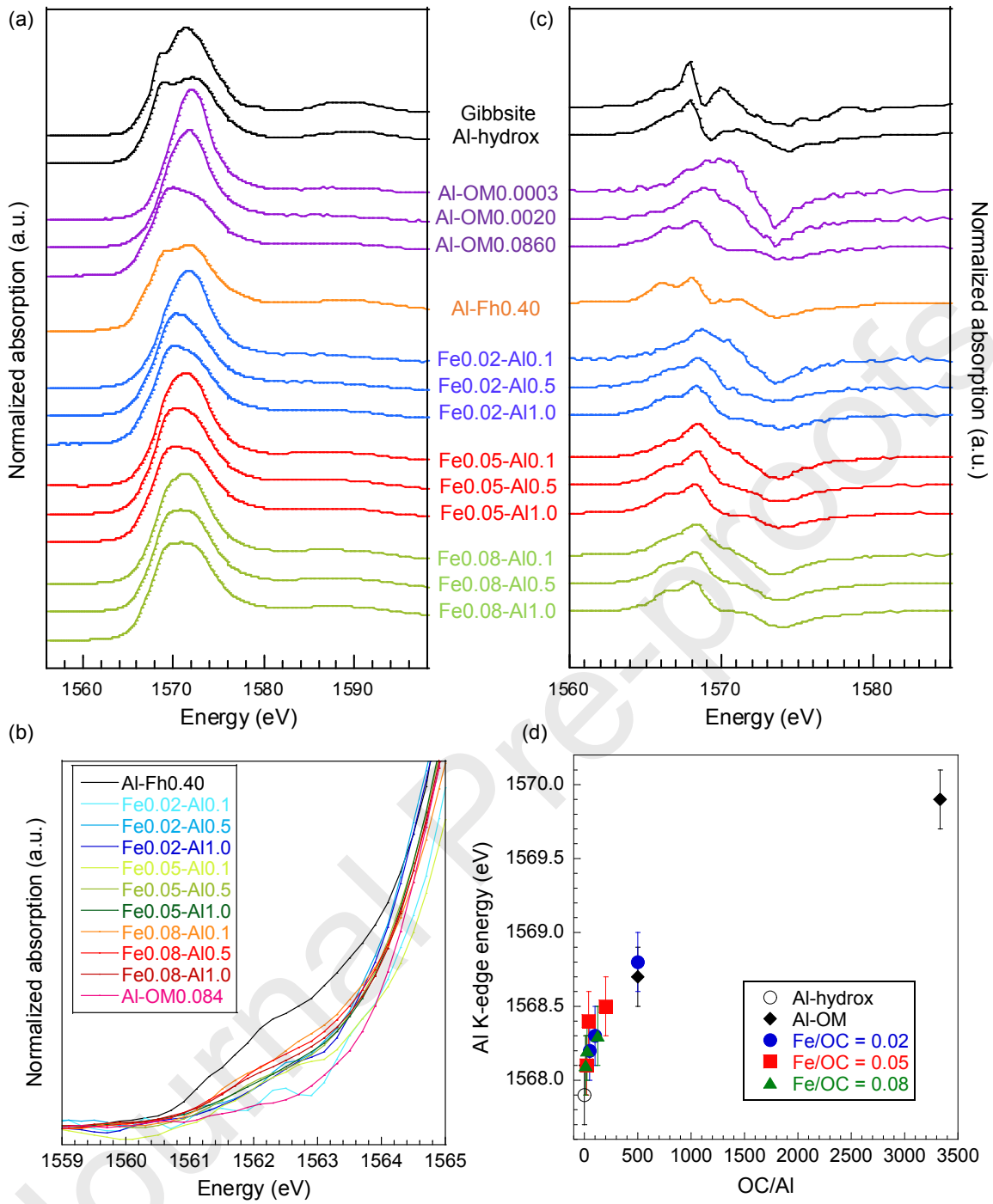

Figure 2 – (a) Al K-edge XANES spectra of the samples and references, (b) zoom of the pre-edge region between 1559 and 1565 eV, (c) first derivatives of the Al K-edge XANES spectra. (d) Evolution of the edge position relative to the OC/Al ratio for Al-hydrox (black empty circles), Al-OM references (black diamonds), and Fe-OM-Al aggregates with Fe/OC = 0.02 (blue circles), 0.05 (red squares) and 0.08 (green triangles). The error on the Al K-edge energy was determined to be +/-0.2 eV as it was the acquisition step used to record data.

3.2. Fe speciation within Fe-OM-Al aggregates

The speciation of Fe within Fe-OM-Al aggregates was investigated by XAS at the Fe K-edge. All of the XANES spectra exhibited a white line at ~ 7128 eV and a shape that is representative of Fe(III) in an octahedral symmetry (Wilke et al., 2001) (Figure S2). All of the EXAFS spectra exhibited a maximum amplitude at k ~ 6.3 $Å^{-1}$. The Fe(III)-oligomer EXAFS signal showed a quasi-monotonous damping shape. In the signal of the Fh, the small-Fh and the three references 'Fh-like Np', a shoulder and a marked feature occurred at ~5.1 $Å^{-1}$ and ~7.5 $Å^{-1}$, respectively. The same trend was observed for Fe-OM-Al aggregates with Fe/OC ≥ 0.05 while the samples with Fe/OC = 0.02 were less structured since only a small shoulder occurs at ~ 5.1 $Å^{-1}$ (Figure 3).

In recent studies, it has been demonstrated that the Fe K-edge EXAFS signal of Fe-OM-Ca aggregates with Fe/OC = 0.05 and 0.08 can be correctly reproduced using Fe(III)-oligomers, small-Fh and Fh as references (Figure S3) (Beauvois et al., 2020). The EXAFS spectra of Fh exhibited a more structured shape than that of small-Fh. The fitting of the EXAFS spectra by Vantelon et al. (2019) reported that small-Fh exhibits respectively more O and less Fe atoms in the first and second coordination shell of Fe than the fit of the Fh. They assumed that these discrepancies by are relevant of a smaller size of particle for small-Fh (referred as Cpt-3 in the mentioned study) than that of Fh. The EXAFS signal of Fe-OM-Al aggregates with Fe/OC = 0.05 and 0.08 was analyzed by performing LCF using the above mentioned three references (Figure 3). However, for Fe/OC = 0.02, some discrepancies were observed between the raw signal of samples and the LCF using Fe(III)-oligomers, small-Fh and Fh (data not shown). Beauvois et al. (2021) observed the same behavior with Ca and they explained this observation by the fact that the small-Fh size were too large compared to the one within the sample. This resulted in the absence of a marked feature at 7.5 $Å^{-1}$. Beauvois et al. (2021) implemented a method to extract the EXAFS signal representative of a Fh-like nanoparticle for Ca/Fe = 0.0,

0.5 and 1.0. Here, we therefore used the above mentioned signal of Fh-like nanoparticles and Fe(III)-oligomers to fit the EXAFS of Fe-OM-Al aggregates with Fe/OC = 0.02 (Figure 3).

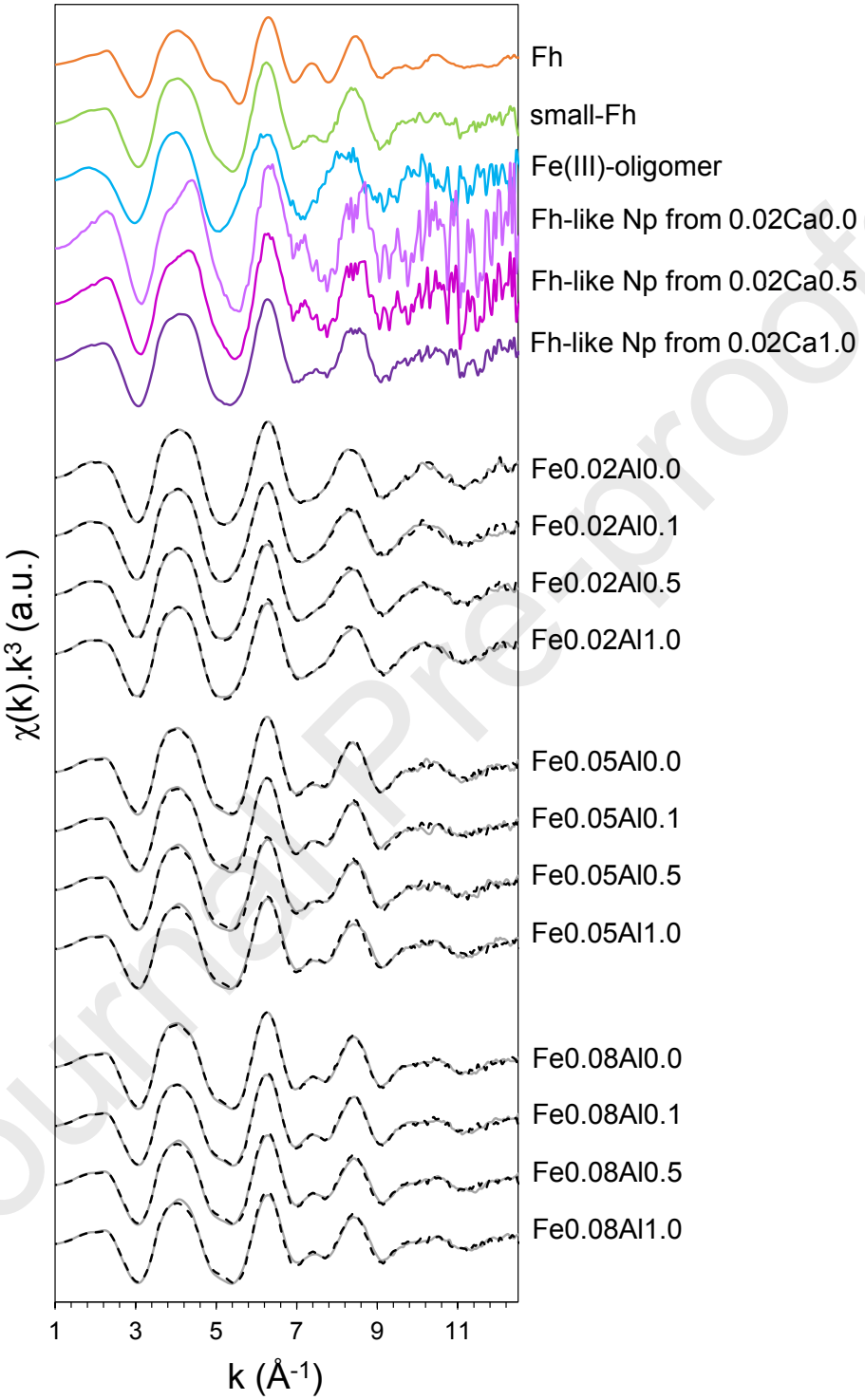

Figure 3 – EXAFS signal at the Fe K-edge of references used to perform LCF and of the Fe-OM-Al aggregates. The spectra of Fe(III)-oligomer and small-Fh come from study by Vantelon et al. (2019). The three references 0.02Ca0.0, 0.02Ca0.1 and 0.02Ca1.0 come from the study by Beauvois et al. (2021).The gray solid lines represent the experimental data of Fe-OM-Al aggregates and the black dotted lines represent the LCF results.

The final proportion of Fe(III)-oligomers, small-Fh and Fh within the Fe-OM-Al aggregates are reported in Figure 4. The results demonstrated a decrease in the proportion of Fe(III)-oligomers with the increasing Fe/OC ratios and for the lowest Fe/OC ratio with the increasing Al/Fe ratios. For Fe/OC ≥ 0.05, the percentage of Fe(III)-oligomers remained constant (~20%) irrespective of the Al/Fe ratios and the proportion of Fh increased with both the increasing Fe/OC and Al/Fe ratios at the expense of small-Fh. These findings indicate an increase in the amount of large Fh nanoparticles with the increasing Fe and Al content within Fe-OM-Al aggregates.

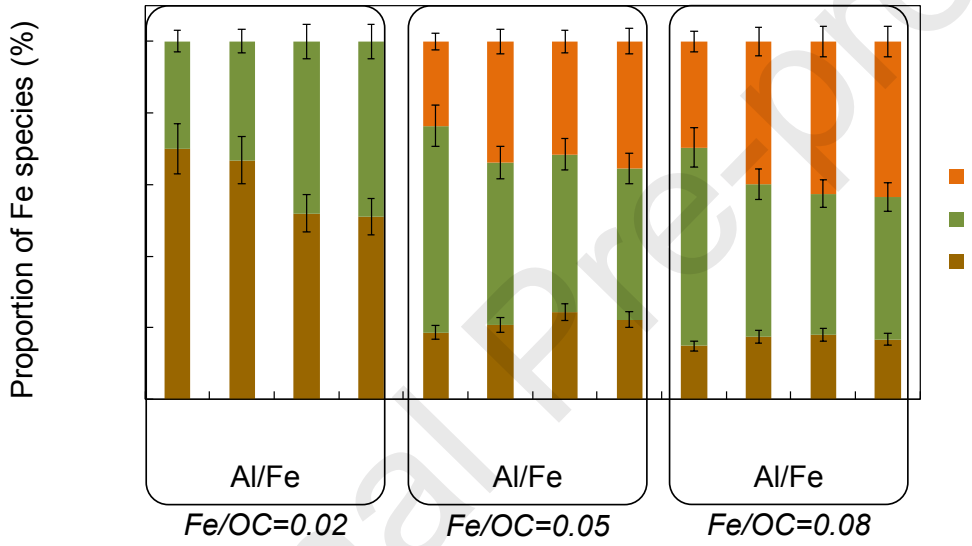

Figure 4 – Proportion of Fe(III)-oligomers (brown), small-Fh (green) and Fh (orange) occurring in the Fe-OM-Al aggregates. The error bars were set to ±10% as described in the materials and methods section.

3.3. Organization of Fe(III) particles within Fe-OM-Al aggregates

To go deeper in the organization of Fh-like Nps (i.e. small-Fh and Fh), we performed SAXS measurements, which allowed to investigate only the Fe particulate part of the Fe-OM-Al aggregates, (Figure 5). Between 2×10^{-1} and 1×10^{-2} $Å^{-1}$, the SAXS curves exhibited a shoulder, relevant of the form factor describing the size and the shape of particles (Guinier et al., 1955), as previously observed for Fe-OM(-Ca) aggregates (Guénet et al., 2017; Beauvois et al., 2020) and Fe/Cr-OM associations (Deng et al., 2021). The shoulder shifted to the low q values with the increasing Al/Fe ratio which indicated a modification of the form factor. This

observation is due to an increase in the size of the particles. For Fe/OC = 0.02, the inflexion of the curve was stronger with Al than without Al whereas for Fe/OC ≥ 0.05, it was weaker for high Al contents compared to low Al contents. In the low q domain, the scattered intensity increased according to a $q^{-2.4}$ power law, which indicated the occurrence of larger structures resulting from the aggregation of the particles (Pignon et al., 1997; Michot et al., 2013). However, no plateau was observed at low q values, meaning that the size of this aggregate was too large for the q range reached by the SAXS configuration which allowed to probe structures between 0.8-300 nm.

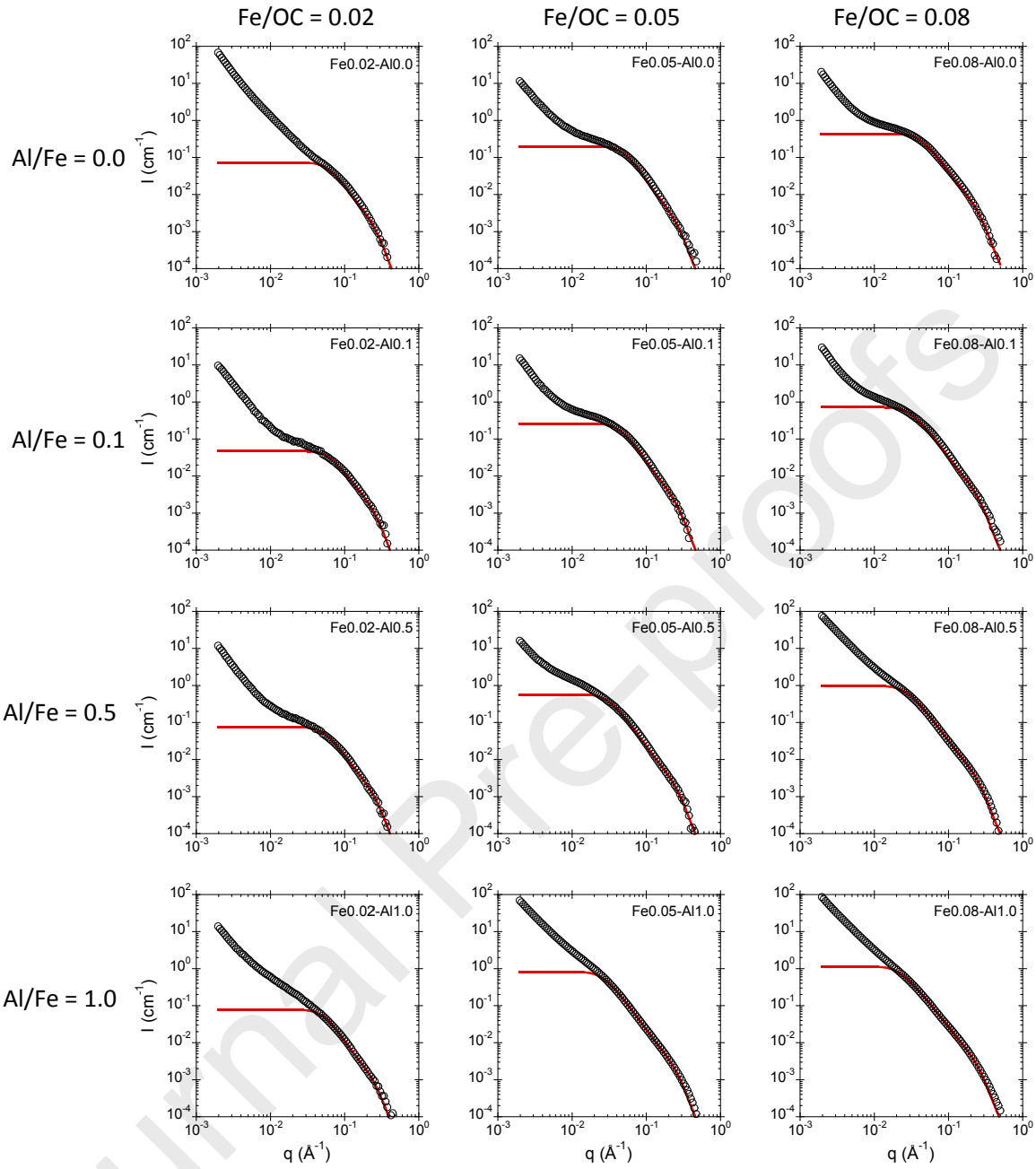

Figure 5 – SAXS curves (black empty circles) and the modelled Fh-like Nps form factor (red line) for the Fe-Al-OM aggregates.

To thoroughly investigate the organization of the Fh-like Nps, we used the model described in the materials and methods to fit the SAXS curves. The form factor of the Fh-like Nps, referred as Fe primary aggregates (Fe-PA) in the model, was calculated from a spherical form factor of a base unit that composed the ferrihydrite particles, referred as Fe primary bead (Fe-PB) in the model (Figure 5). The size of this base unit was adjusted to 0.8 nm in radius by

fitting properly the high q domain of the SAXS curves as previously proposed (Guénet et al., 2017), and is in accordance with the size of the coherence scattering domain of Fh evidenced by Michel et al. 2007. The radius of the Fh-like Nps ($R_{Fh\text{-}Nps}$) was calculated from the form factor (P(q)) (Figure 6). The results demonstrated an increase in the Fh-like Nps size with the increasing Fe/OC ratio, as previously observed (Guénet et al., 2017; Beauvois et al., 2020). Moreover, $R_{Fh\text{-}Nps}$ increased with the increasing Al/Fe ratio. However, the Fh-like Nps fractal dimension (D_f) remained constant at 2.4 ± 0.2 irrespective of the Fe/OC or Al/Fe ratios, highlighting their stable morphology.

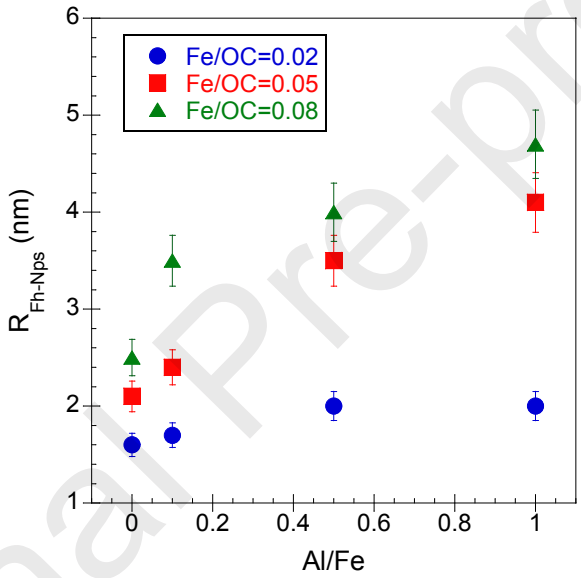

Figure 6 – Evolution of $R_{Fh\text{-}Nps}$ relative to the Al/Fe ratio for Fe/OC = 0.02 (blue circles), Fe/OC = 0.08 (red squares) and Fe/OC = 0.08 (green triangles). The errors bars were set to 15 % by checking the accuracy of the fit modifying the parameters.

The apparent total structure ($S_T(q)$) was extracted by dividing the total scattered intensity by the P(q) of Fh-like Nps (Figure S4). The obtained $S_T(q)$ exhibited an increasing intensity at low q values that was representative of a larger structure composed by the aggregation of Fh-like Nps, referred as Fe secondary aggregate in the model. Unfortunately, no plateau was observed at low q and we were not able to calculate the size of this aggregate. However, the shoulder occurring at ~ 10^{-1} $Å^{-1}$ for the lowest Fe/OC and Al/Fe ratios is representative of an interaction between Fh-like Nps within the aggregate. The position of this

shoulder allows to estimate the center-to-center distance, d_0, between two Fh-like Nps (Table 2). The increase in d_0 with the increasing Fe/OC and Al/Fe ratios is due to the increase in the Fh-like Nps size since d_0 was calculated to be ~ $2.4 \times R_{Fe\text{-}PA}$. The key result is observed for the three higher Al content samples for which no shoulder was observed suggesting an increase in d_0 and/or its polydispersity. Therefore, the increasing Al/Fe ratio leads to an increase in the range correlation between Fh-like Nps.

Table 2 – Center-to-center distance, d_0, between two Fh-like Nps. The symbol '-' is used when no shoulder was observed in $S_T(q)$ indicating high d_0 values.

d0 (nm)		Al/Fe 0.0	0.1	0.5	1.0
Fe/OC	**0.02**	4.4	4.8	5.0	5.0
	0.05	5.2	5.7	7.0	-
	0.08	4.5	7.0	-	-

3.4. Overall organization of Fe-OM-Al aggregates

To probe the hundreds nm scale organization of Fe-OM-Al aggregates, we performed cryo-TEM observations (Figure 7). The image of Fe0.08-Al0.1 exhibited a homogeneous background with dispersed black dots of the order of nm in size, which is consistent with the one of Fh-like Nps previously calculated by SAXS (Figure 7a). This observation is consistent with the stable colloidal suspension of Fe0.08-Al0.1 (Figure 1). By contrast, the image of Fe0.08-Al1.0 is heterogenous. The bottom-right hand corner of the image displayed a continuous light-gray background demonstrated that no sample was present in this part. On the contrary, the top left-hand corner revealed black dots embedded in a dark background. This feature is relevant of the occurrence of a large structure of the order of µm in size composed of Fh-like Nps embedded in an OM matrix, as previously observed for Fe-OM-Ca aggregates (Beauvois et al., 2020). These observations demonstrated that, for the highest [Al], an OM micrometric network in which Fh-like Nps are embedded is formed leading to the settlement of the aggregates (Figure 1).

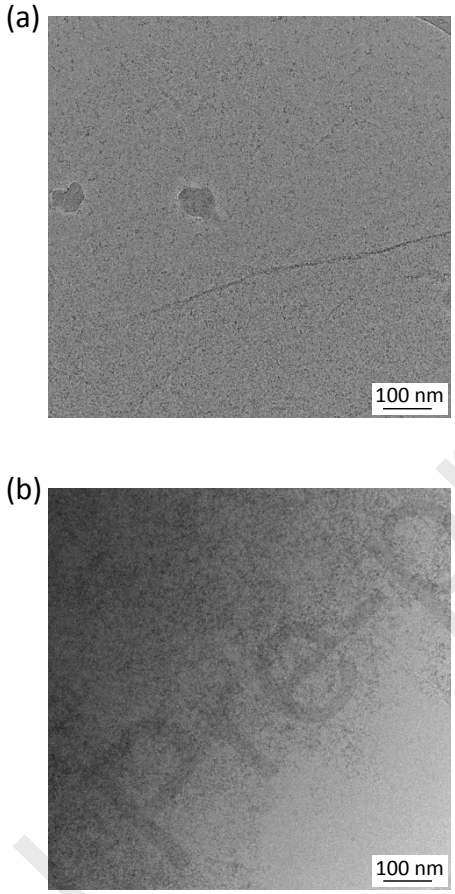

Figure 7 – Cryo-TEM images of (a) Fe0.08-Al0.1 and (b) Fe0.08-Al1.0. In (a), the two dark gray spots are surrounded by a white hallo indicating that they are not in the focalization plane: these features represent pollution and are not part of the Fe0.08-Al0.1 sample.

4. Discussion

Aluminum interacted with both the OM and Fe parts of the Fe-OM aggregates. With regards to the interaction of Al with OM, several authors have already demonstrated the ability of Al to be bound by OM colloids *via* their carboxylic sites (Lippold et al., 2005; Tipping, 2005; Marsac et al., 2012; Adusei-Gyamfi et al., 2019). This binding limits the Al polymerization as previously observed for crystal growth in Fe oxyhydroxides (Karlsson and Persson, 2010; Pédrot et al., 2011; Guénet et al., 2017; Vantelon et al., 2019). Consequently, at low concentration, Al was mainly organized as monomers and/or small oligomers bound to OM.

The slight structuration of the Al K-edge XANES spectra and the energy shift of the edge demonstrated that Al polymerization increased with increasing [Al] (Figure 2). Iron was organized as Fe(III)-oligomers and Fh-like Nps of various sizes regardless of the Al content. The binding of Al by OM partially limits the Fe interactions with OM and allows the size of Fh-like Nps to increase.

Aluminum also interacted with the Fe phases, as highlighted by the pre-edge observed on the Al k-edge XANES spectra (Figure 2c). Aluminum is known to incorporate Fe oxyhydroxides without modifying the structure of the Fe phases (Hazemann et al., 1991; Hansel et al., 2011; Cismasu et al., 2012; Adra et al., 2013). The relative constant pre-edge intensity and the edge shift suggested that the same Al fraction is involved in the Al-O-Fe bonds despite the variation in the polymerization rate.

Based on these results, we propose a schematic evolution of the structure of the Fe-OM aggregates as a function of the Al concentration. Whatever the Al content, the Fe mineral phases within the Fe-OM-Al aggregates are the same, i.e. Fe(III)-oligomers and Fh-like Nps. However, their proportion and the size of Fh-like Nps, as well as the OM organization strongly depend on Al concentration. For low [Al] (< 1.5 mmol L^{-1}), the Fe-OM-Al associations were organized as colloidal aggregates. The Fe phases were distributed as Fe(III)-oligomers and small Fh-like Nps, all bound to OM, exhibiting the same fractal organization as previously described (Guénet et al., 2017; Beauvois et al., 2020) (Figure 8). In this system, Al is distributed following the same scheme, in which monomers and oligomers, bound to OM, dominate. For high [Al] (> 2.0 mmol L^{-1}), Fe-OM-Al associations form a non-colloidal system in which small Al polymers bound to OM are predominant due to the polymerization of Al monomers and oligomers. In such conditions, Fe is distributed as Fe(III)-oligomers and Fh-like Nps bound to OM. The content and size of the Fh-like Nps is higher for high [Al] than for low [Al], as a consequence of the interaction between Al and OM which is therefore less available to limit the growth of

Fh-like Nps. In the presence of high amount of humic acid, Fh nanoparticles are not expected to aggregate, as explained by the DLVO theory (Liu et al., 2019). The same trend is observed in this study, and the sedimentation of Fe-OM-Al aggregates at high (Fe+Al) concentrations is due to the formation of a huge OM micrometric network in which Fe and Al species are embedded (Figure 8). The high amounts of Al control a structural transition of the global size of the Fe-OM aggregates and affect their colloidal stability.

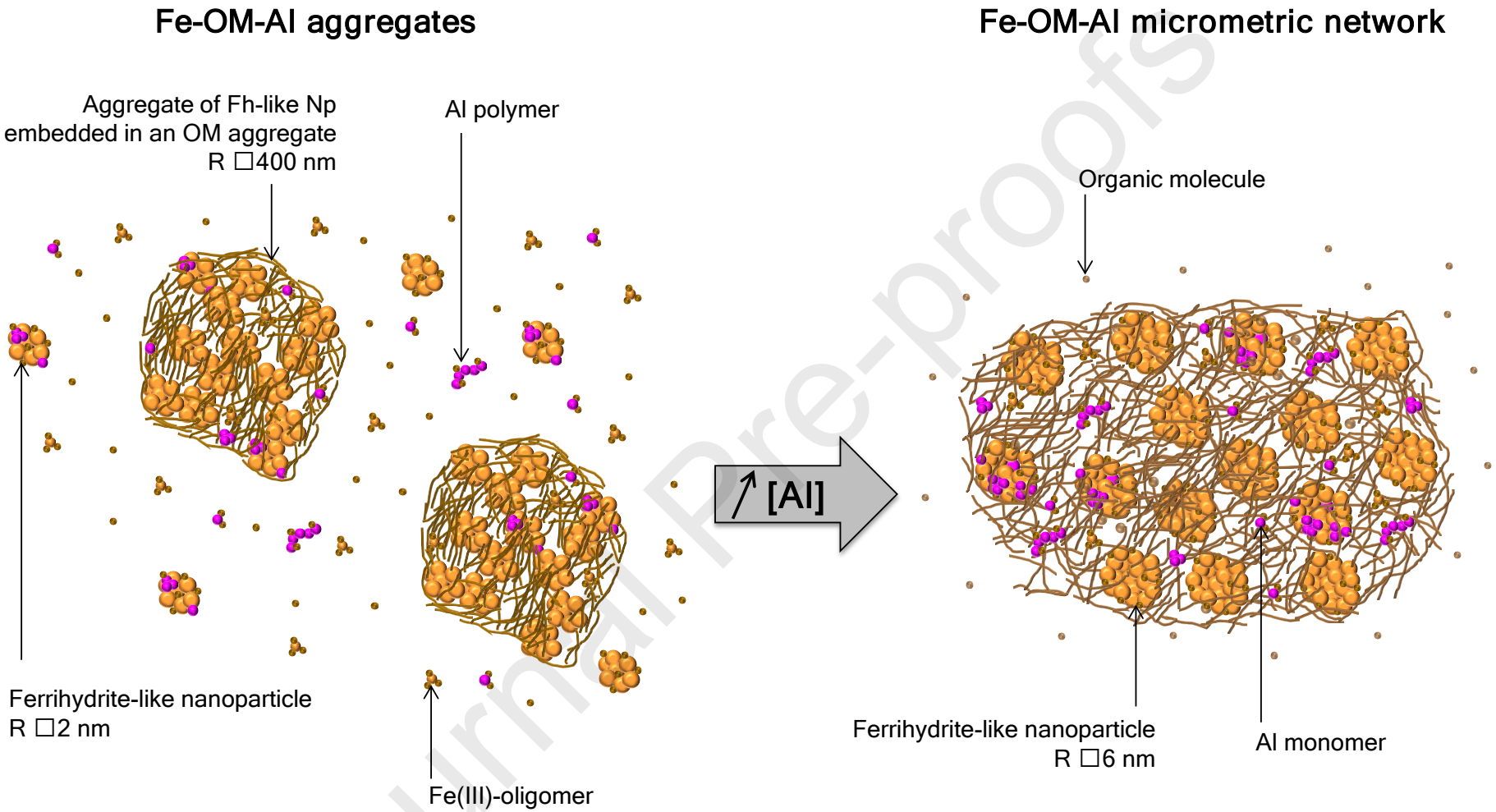

Figure 8 – Schematic representation of the structural organization of the Fe-OM-Al modification with an increasing Al concentration.

This described structural organization of Fe-OM aggregates could have a major impact on the global reactivity of the aggregates. Aluminum oxyhydroxides are known to adsorb pollutants (Islam et al., 2018) such as arsenic (Mertens et al., 2016). Moreover, mixed Al(III)-Fe(III) oxyhydroxides exhibit a higher sorption capacity for phosphate (Harvey and Rhue, 2008), chromate (Ni et al., 2016), sulfate (Namayandeh and Kabengi, 2019) and arsenate (Adra et al., 2013) than Fe(III) oxyhydroxides. An increase in the overall aggregates sorption capacity towards pollutants which exhibit high affinity for mineral phases with an increasing [Al] is therefore expected. Moreover, the settling of the Fe-OM aggregates with increasing [Al] will immobilize the pollutants that have potentially been adsorbed at their surface by physically retaining large aggregates in soil porous media (Kretzschmar and Schäfer, 2005). In recent studies, the co-precipitation of Fe(III), Cr(III) and OM was investigated (Xia et al., 2022 and references herein). They demonstrated that the immobilization of Cr(III), mainly bound to Fe (oxy)hydroxides, is inhibited for the higher Fe/OC molar ratio they used, i.e. equal to 0.05. Authors explain this observation by the formation of soluble OM-Fe(III)-Cr(III) complexes. With our work, we can hypothesize that the presence of Al(III) in such system would have the opposite effect. Thanks to Al interaction with the OM part, more Fh-like Nps binding sites would be thus available to bind Cr(III) and the formation of the huge micrometric network will help to immobilized the adsorbed Cr(III), as discussed above.

With regards to their reactivity to bioreduction, Lovley et al. (1996) reported that OM acts as an electron shuttle in the bioreduction of Fe(III)-OM colloids resulting in a faster transformation for OM embedded Fe oxyhydroxides than for particulate Fe oxyhydroxides. Ekstrom et al. (2010) demonstrated that the Fe(III) bioreduction rate of Al substituted ferrihydrite was lower than for Fh and Masue-Slowey et al. (2011) explained that the presence of Al^{3+} in the Fh structure inhibits the transfer of electron. Therefore, OM and Al have an

opposite impact on Fe(III) reduction. This raises the question of how the concomitant presence of Al and OM could affect the bioreduction rate of Fe within these organo-mineral aggregates.

In environmental systems, Al prevails alongside other cations such as Ca, which is of major importance regarding its high abundance (Iglesias et al., 2003). Recently, Beauvois et al. (2020) demonstrated that the global impact of Ca on the colloidal stability of Fe-OM aggregates is the same as for Al: at high cations concentration, the Fe-OM-cation aggregates settled as a consequence of the formation of a huge micrometric network. However, the mechanisms involved are different: Ca only interacts with OM while Al interacts with both OM and Fe phases. More precisely, when Fe, Ca and OM coprecipitate, even if the affinity of Ca for OM is significantly lower than that of Fe-oxyhydroxides (Milne et al., 2003; Cabaniss, 2009), Ca occurred as dimers only bound to OM (Davis and Edwards, 2017; Adhikari et al., 2019; Beauvois et al., 2020). As for Ca, Al exhibits a much lower affinity for OM than for Fe (Nierop et al., 2002; Milne et al., 2003; Cabaniss, 2009). The affinity constant of Al and Fe towards carboxylic groups of humic acid was calculated to be $\sim 10^{-1}$ and $\sim 10^{3}$, respectively (Milne et al., 2003). In contrast to Ca, during the coprecipitation of Fe, Al and OM, Al interacts with both OM and Fe as demonstrated in the present study and other works (Nierop et al., 2002; Pokrovsky et al., 2005). Under environmental conditions, cations generally occur together, which raises questions on their concomitant impact on the structure of Fe-OM aggregates. The binding strength with OM is slightly higher for Al than for Ca (Milne et al., 2003; Cabaniss, 2009). The affinity constant of Ca towards carboxylic groups of humic acid was calculated to be $\sim 10^{-1.4}$ (Milne et al., 2003). Therefore, when Fe, Al, Ca and OM occur together, OM is expected to preferentially bind Fe > Al > Ca. Studying Fe-Al-organic colloids from peat soil solutions Pokrovsky et al. (2005) observed that Ca^{2+} was mainly distributed in dissolved fractions for low [OM]. However, for higher organic-rich waters in the boreal area, Pokrovsky and Schott (2002) provided evidence that Ca was associated with organic colloids. Moreover,

the variation in [Ca] within natural systems leads to a variation in the ionic strength, a major controlling parameter for the organization of Fe-OM aggregates. The structural arrangement between Fe and OM when various additional ions such as Al and Ca occur simultaneously then appears to be complex and should therefore be further investigated.

5. Conclusion

In this study, the impact of Al on the structural organization of Fe-OM aggregates was investigated. The Al occurrence does not modify the nature of Fe phases which are always organized as Fe(III)-oligomers and Fh-like Nps. However, at high [Al], more Fh-like Nps are formed and their size is higher than for low [Al]. These results shed new light on the understanding of the impact of major ions, such as Al, on Fe-OM aggregates which are recognized as a key parameter controlling chemical elements in the environmental biogeochemical cycle. Aluminum interacted with both Fe and OM and was distributed as Al monomers, oligomers and small polymers, all bound to OM. The polymerization rate of Al increased with the increasing Al concentration. At high Al and Fe concentration, Fe-OM-Al aggregates moved from a colloidal to a settling system. Aluminum polymers offered new reactive sites for binding pollutants. Moreover, the sorption capacity of Fe nanoparticles should increase in response to the decrease in OM binding and subsequent increase in the Fe nanoparticle functional group availability. The transfer/transport of adsorbed pollutants is therefore controlled by the presence of major ions such as Al that control the transition between a colloidal and particle regime. These original results shed new light on the impact of major ions and on their simultaneous presence in the structural organization of Fe-OM aggregates. Further studies must be performed to understand if their individual impact on the structural organization of Fe-OM is additive or competitive. With respect to the competitive impact, the hypothesis that Al would have the most influence seems to be the most probable since OM preferentially binds Al rather than Ca, for instance. Moreover, in such conditions, the impact of

variations in the ionic strength (subsequent to additional environmental major ions such as Ca), on the structural organization of the Fe-OM aggregates is called into question.

Acknowledgments

This study is part of a PhD project funded by the French administrative region of Brittany and by SOLEIL synchrotron-LLB through the "ORPHREA" project. This study was funded by the French "Institut national des sciences de l'Univers" (INSU) through the "Initiative Structurante EC2CO – BIOHEFECT" allocated to "DV" via the 'ISAAP' project. The authors are grateful to Karine Chaouchi for performing ICP-OES analysis. The authors acknowledge SOLEIL for beamtime allocation at the LUCIA beamline (proposal 99170211) and ROCK beamline (proposal 20170795). The work at ROCK was supported by a public grant overseen by the French National Research Agency (ANR) as a part of the "Investissements d'Avenir" program ref: ANR-10-EQPX-45. Dr. Sara Mullin is acknowledged for post-editing the English style.

Appendix A. Supplementary material

The supplementary material for this article includes elemental composition of Fe-OM-Al aggregates, the XRD characterization of references. Readers will also find additional information dealing with XAS at the Fe K-edge: the XANES spectra, the EXAFS spectra used for LCF and tables reporting the results of the LCF. Finally, the results of SAXS curves fitting are also presented in the supplementary material. Research data are also available (as a CSV file).

References

Adhikari D., Sowers T., Stuckey J. W., Wang X., Sparks D. L. and Yang Y. (2019) Formation and redox reactivity of ferrihydrite-organic carbon-calcium co-precipitates. *Geochim. Cosmochim. Acta* **244**, 86–98.

Adra A., Morin G., Ona-Nguema G. and Brest J. (2016) Arsenate and arsenite adsorption onto Al-containing ferrihydrites. Implications for arsenic immobilization after neutralization of acid mine drainage. *Appl. Geochem.* **64**, 2–9.

Adra A., Morin G., Ona-Nguema G., Menguy N., Maillot F., Casiot C., Bruneel O., Lebrun S., Juillot F. and Brest J. (2013) Arsenic Scavenging by Aluminum-Substituted Ferrihydrites

in a Circumneutral pH River Impacted by Acid Mine Drainage. *Environ. Sci. Technol.* **47**, 12784–12792.

Adusei-Gyamfi J., Ouddane B., Rietveld L., Cornard J.-P. and Criquet J. (2019) Natural organic matter-cations complexation and its impact on water treatment: A critical review. *Water Res.* **160**, 130–147.

Beaucage G. (1996) Small-Angle Scattering from Polymeric Mass Fractals of Arbitrary Mass-Fractal Dimension. *J. Appl. Crystallogr.* **29**, 134–146.

Beauvois A., Vantelon D., Jestin J., Bouhnik-Le Coz M., Catrouillet C., Briois V., Bizien T. and Davranche M. (2021) How crucial is the impact of calcium on the reactivity of iron-organic matter aggregates? Insights from arsenic. *J. Hazard. Mater.* **404**, 124127.

Beauvois A., Vantelon D., Jestin J., Rivard C., Bouhnik-Le Coz M., Dupont A., Briois V., Bizien T., Sorrentino A., Wu B., Appavou M.-S., Lotfi-Kalahroodi E., Pierson-Wickmann A.-C. and Davranche M. (2020) How does calcium drive the structural organization of iron–organic matter aggregates? A multiscale investigation. *Environ. Sci. Nano* **7**, 2833–2849.

Bi S. (2004) Studies on the mechanism of hydrolysis and polymerization of aluminum salts in aqueous solution: correlations between the "Core-links" model and "Cage-like" Keggin-Al13 model. *Coord. Chem. Rev.* **248**, 441–455.

Briois V., La Fontaine C., Belin S., Barthe L., Moreno T., Pinty V., Carcy A., Girardot R. and Fonda E. (2016) ROCK: the new Quick-EXAFS beamline at SOLEIL. *J. Phys. Conf. Ser.* **712**, 012149.

Cabaniss S. E. (2009) Forward Modeling of Metal Complexation by NOM: I. *A priori* Prediction of Conditional Constants and Speciation. *Environ. Sci. Technol.* **43**, 2838–2844.

Cismasu A. C., Michel F. M., Stebbins J. F., Levard C. and Brown G. E. (2012) Properties of impurity-bearing ferrihydrite I. Effects of Al content and precipitation rate on the structure of 2-line ferrihydrite. *Geochim. Cosmochim. Acta* **92**, 275–291.

Davis C. C. and Edwards M. (2017) Role of Calcium in the Coagulation of NOM with Ferric Chloride. *Environ. Sci. Technol.* **51**, 11652–11659.

Deng N., Li Z., Zuo X., Chen J., Shakiba S., Louie S. M., Rixey W. G. and Hu Y. (2021) Coprecipitation of Fe/Cr Hydroxides with Organics: Roles of Organic Properties in Composition and Stability of the Coprecipitates. *Environ. Sci. Technol.* **55**, 4638–4647.

Dia A., Gruau G., Olivié-Lauquet G., Riou C., Molénat J. and Curmi P. (2000) The distribution of rare earth elements in groundwaters: assessing the role of source-rock composition, redox changes and colloidal particles. *Geochim. Cosmochim. Acta* **64**, 4131–4151.

Ducher M., Blanchard M., Vantelon D., Nemausat R. and Cabaret D. (2016) Probing the local environment of substitutional Al^{3+} in goethite using X-ray absorption spectroscopy and first-principles calculations. *Phys. Chem. Miner.* **43**, 217–227.

Ekstrom E. B., Learman D. R., Madden A. S. and Hansel C. M. (2010) Contrasting effects of Al substitution on microbial reduction of Fe(III) (hydr)oxides. *Geochim. Cosmochim. Acta* **74**, 7086–7099.

Flank A.-M., Cauchon G., Lagarde P., Bac S., Janousch M., Wetter R., Dubuisson J.-M., Idir M., Langlois F., Moreno T. and Vantelon D. (2006) LUCIA, a microfocus soft XAS beamline. *Nucl. Instrum. Methods Phys. Res. Sect. B Beam Interact. Mater. At.* **246**, 269–274.

Guénet H., Davranche M., Vantelon D., Gigault J., Prévost S., Taché O., Jaksch S., Pédrot M., Dorcet V., Boutier A. and Jestin J. (2017) Characterization of iron–organic matter nano-aggregate networks through a combination of SAXS/SANS and XAS analyses: impact on As binding. *Environ. Sci. Nano* **4**, 938–954.

Guénet H., Davranche M., Vantelon D., Pédrot M., Al-Sid-Cheikh M., Dia A. and Jestin J. (2016) Evidence of organic matter control on As oxidation by iron oxides in riparian wetlands. *Chem. Geol.* **439**, 161–172.

Guinier A., Fournet G. and Yudowitch K. L. (1955) *Small-angle scattering of X-rays*., Wiley New York.

Hagvall K., Persson P. and Karlsson T. (2015) Speciation of aluminum in soils and stream waters: The importance of organic matter. *Chem. Geol.* **417**, 32–43.

Hansel C. M., Learman D. R., Lentini C. J. and Ekstrom E. B. (2011) Effect of adsorbed and substituted Al on Fe(II)-induced mineralization pathways of ferrihydrite. *Geochim. Cosmochim. Acta* **75**, 4653–4666.

Harvey O. R. and Rhue R. D. (2008) Kinetics and energetics of phosphate sorption in a multi-component Al(III)–Fe(III) hydr(oxide) sorbent system. *J. Colloid Interface Sci.* **322**, 384–393.

Hay M. B. and Myneni S. C. B. (2010) X-ray Absorption Spectroscopy of Aqueous Aluminum-Organic Complexes. *J. Phys. Chem. A* **114**, 6138–6148.

Hazemann J.-L., Bérar J. F. and Manceau A. (1991) Rietveld Studies of the Aluminium-Iron Substitution in Synthetic Goethite. *Mater. Sci. Forum* **79–82**, 821–826.

Hirst C., Andersson P. S., Shaw S., Burke I. T., Kutscher L., Murphy M. J., Maximov T., Pokrovsky O. S., Mörth C.-M. and Porcelli D. (2017) Characterisation of Fe-bearing particles and colloids in the Lena River basin, NE Russia. *Geochim. Cosmochim. Acta* **213**, 553–573.

Hofmann A., Vantelon D., Montargès-Pelletier E., Villain F., Gardoll O., Razafitianamaharavo A. and Ghanbaja J. (2013) Interaction of Fe(III) and Al(III) during hydroxylation by forced hydrolysis: The nature of Al–Fe oxyhydroxy co-precipitates. *J. Colloid Interface Sci.* **407**, 76–88.

Hu Y. F., Xu R. K., Dynes J. J., Blyth R. I. R., Yu G., Kozak L. M. and Huang P. M. (2008) Coordination nature of aluminum (oxy)hydroxides formed under the influence of tannic acid studied by X-ray absorption spectroscopy. *Geochim. Cosmochim. Acta* **72**, 1959–1969.

Iglesias A., López R., Fiol S., Antelo J. M. and Arce F. (2003) Analysis of copper and calcium–fulvic acid complexation and competition effects. *Water Res.* **37**, 3749–3755.

Ildefonse P., Cabaret D., Sainctavit P., Calas G., Flank A.-M. and Lagarde P. (1998) Aluminium X-ray absorption Near Edge Structure in model compounds and Earth's surface minerals. *Phys. Chem. Miner.* **25**, 112–121.

Islam Md. A., Morton D. W., Johnson B. B., Pramanik B. K., Mainali B. and Angove M. J. (2018) Metal ion and contaminant sorption onto aluminium oxide-based materials: A review and future research. *J. Environ. Chem. Eng.* **6**, 6853–6869.

Karlsson T. and Persson P. (2010) Coordination chemistry and hydrolysis of Fe(III) in a peat humic acid studied by X-ray absorption spectroscopy. *Geochim. Cosmochim. Acta* **74**, 30–40.

Karlsson T., Persson P., Skyllberg U., Mörth C.-M. and Giesler R. (2008) Characterization of Iron(III) in Organic Soils Using Extended X-ray Absorption Fine Structure Spectroscopy. *Environ. Sci. Technol.* **42**, 5449–5454.

Kim J., Ilott A. J., Middlemiss D. S., Chernova N. A., Pinney N., Morgan D. and Grey C. P. (2015) ^{2}H and ^{27}Al Solid-State NMR Study of the Local Environments in Al-Doped 2-Line Ferrihydrite, Goethite, and Lepidocrocite. *Chem. Mater.* **27**, 3966–3978.

Klöppel H., Fliedner A. and Kördel W. (1997) Behaviour and ecotoxicology of aluminium in soil and water - Review of the scientific literature. *Chemosphere* **35**, 353–363.

Kretzschmar R. and Schäfer T. (2005) Metal Retention and Transport on Colloidal Particles in the Environment. *Elements* **1**, 205–210.

Liao S., Wang X., Yin H., Post J. E., Yan Y., Tan W., Huang Q., Liu F. and Feng X. (2020) Effects of Al substitution on local structure and morphology of lepidocrocite and its phosphate adsorption kinetics. *Geochim. Cosmochim. Acta* **276**, 109–121.

Lippold H., Mansel A. and Kupsch H. (2005) Influence of trivalent electrolytes on the humic colloid-borne transport of contaminant metals: competition and flocculation effects. *J. Contam. Hydrol.* **76**, 337–352.

Liu J., Louie S. M., Pham C., Dai C., Liang D. and Hu Y. (2019) Aggregation of ferrihydrite nanoparticles: Effects of pH, electrolytes,and organics. *Environ. Res.* **172**, 552–560.

Lotfi-Kalahroodi E., Pierson-Wickman A.-C., Guenet H., Rouxel O., Ponzevera E., Bouhnik-Le Coz M., Vantelon D., Dia A. and Davranche M. (2019) Iron isotope fractionation in iron-organic matter associations: Experimental evidence using filtration and ultrafiltration. *Geochim. Cosmochim. Acta* **250**, 98–116.

Lovley D. R., Coates J. D., Blunt-Harris E. L., Phillips E. J. P. and Woodward J. C. (1996) Humic substances as electron acceptors for microbial respiration. *Nature* **382**, 445–448.

Marsac R., Davranche M., Gruau G., Dia A. and Bouhnik-Le Coz M. (2012) Aluminium competitive effect on rare earth elements binding to humic acid. *Geochim. Cosmochim. Acta* **89**, 1–9.

Masue-Slowey Y., Loeppert R. H. and Fendorf S. (2011) Alteration of ferrihydrite reductive dissolution and transformation by adsorbed As and structural Al: Implications for As retention. *Geochim. Cosmochim. Acta* **75**, 870–886.

Mertens J., Rose J., Wehrli B. and Furrer G. (2016) Arsenate uptake by Al nanoclusters and other Al-based sorbents during water treatment. *Water Res.* **88**, 844–851.

Michel F. M., Ehm L., Liu G., Han W. Q., Antao S. M., Chupas P. J., Lee P. L., Knorr K., Eulert H., Kim J., Grey C. P., Celestian A. J., Gillow J., Schoonen M. A. A., Strongin D. R. and Parise J. B. (2007) Similarities in 2- and 6-Line Ferrihydrite Based on Pair Distribution Function Analysis of X-ray Total Scattering. *Chem. Mater.* **19**, 1489–1496.

Michot L. J., Bihannic I., Thomas F., Lartiges B. S., Waldvogel Y., Caillet C., Thieme J., Funari S. S. and Levitz P. (2013) Coagulation of Na-Montmorillonite by Inorganic Cations at Neutral pH. A Combined Transmission X-ray Microscopy, Small Angle and Wide Angle X-ray Scattering Study. *Langmuir* **29**, 3500–3510.

Mikutta C. and Kretzschmar R. (2011) Spectroscopic Evidence for Ternary Complex Formation between Arsenate and Ferric Iron Complexes of Humic Substances. *Environ. Sci. Technol.* **45**, 9550–9557.

Milne C. J., Kinniburgh D. G., van Riemsdijk W. H. and Tipping E. (2003) Generic NICA−Donnan Model Parameters for Metal-Ion Binding by Humic Substances. *Environ. Sci. Technol.* **37**, 958–971.

Namayandeh A. and Kabengi N. (2019) Calorimetric study of the influence of aluminum substitution in ferrihydrite on sulfate adsorption and reversibility. *J. Colloid Interface Sci.* **540**, 20–29.

Ni C., Liu S., Cui L., Han Z., Wang L., Chen R. and Liu H. (2016) Adsorption performance of Cr(VI) onto Al-free and Al-substituted ferrihydrites. *RSC Adv.* **6**, 66412–66419.

Nierop K. G. J. J., Jansen B. and Verstraten J. M. (2002) Dissolved organic matter, aluminium and iron interactions: precipitation induced by metal/carbon ratio, pH and competition. *Sci. Total Environ.* **300**, 201–211.

Pédrot M., Boudec A. L., Davranche M., Dia A. and Henin O. (2011) How does organic matter constrain the nature, size and availability of Fe nanoparticles for biological reduction? *J. Colloid Interface Sci.* **359**, 75–85.

Pédrot M., Dia A., Davranche M., Bouhnik-Le Coz M., Henin O. and Gruau G. (2008) Insights into colloid-mediated trace element release at the soil/water interface. *J. Colloid Interface Sci.* **325**, 187–197.

Pignon F., Magnin A., Piau J.-M., Cabane B., Lindner P. and Diat O. (1997) Yield stress thixotropic clay suspension: Investigations of structure by light, neutron, and x-ray scattering. *Phys. Rev. E* **56**, 3281–3289.

Pokrovsky O. S., Dupré B. and Schott J. (2005) Fe–Al–organic Colloids Control of Trace Elements in Peat Soil Solutions: Results of Ultrafiltration and Dialysis. *Aquat. Geochem.* **11**, 241–278.

Pokrovsky O. S. and Schott J. (2002) Iron colloids/organic matter associated transport of major and trace elements in small boreal rivers and their estuaries (NW Russia). *Chem. Geol.* **190**, 141–179.

Ratié G., Vantelon D., Lotfi Kalahroodi E., Bihannic I., Pierson-Wickmann A. C. and Davranche M. (2019) Iron speciation at the riverbank surface in wetland and potential impact on the mobility of trace metals. *Sci. Total Environ.* **651**, 443–455.

Ravel B. and Newville M. (2005) *ATHENA* , *ARTEMIS* , *HEPHAESTUS* : data analysis for X-ray absorption spectroscopy using *IFEFFIT*. *J. Synchrotron Radiat.* **12**, 537–541.

Ritter K., Aiken G. R., Ranville J. F., Bauer M. and Macalady D. L. (2006) Evidence for the Aquatic Binding of Arsenate by Natural Organic Matter−Suspended Fe(III). *Environ. Sci. Technol.* **40**, 5380–5387.

Ščančar J. and Milačič R. (2006) Aluminium speciation in environmental samples: a review. *Anal. Bioanal. Chem.* **386**, 999–1012.

Schwertmann U. and Cornell R. M. eds. (2000) *Iron Oxides in the Laboratary*., Wiley-VCH Verlag GmbH, Weinheim, Germany.

Stolpe B., Guo L., Shiller A. M. and Aiken G. R. (2013) Abundance, size distributions and trace-element binding of organic and iron-rich nanocolloids in Alaskan rivers, as revealed by field-flow fractionation and ICP-MS. *Geochim. Cosmochim. Acta* **105**, 221–239.

ThomasArrigo L. K., Mikutta C., Byrne J., Barmettler K., Kappler A. and Kretzschmar R. (2014) Iron and Arsenic Speciation and Distribution in Organic Flocs from Streambeds of an Arsenic-Enriched Peatland. *Environ. Sci. Technol.* **48**, 13218–13228.

Thurman E. M. (1985) *Organic Geochemistry of Natural Waters*., Springer Netherlands, Dordrecht.

Tipping E. (2005) Modelling Al competition for heavy metal binding by dissolved organic matter in soil and surface waters of acid and neutral pH. *Geoderma* **127**, 293–304.

Vantelon D., Davranche M., Marsac R., La Fontaine C., Guénet H., Jestin J., Campaore G., Beauvois A. and Briois V. (2019) Iron speciation in iron-organic matter nanoaggregates: A kinetic approach coupling Quick-EXAFS and MCR-ALS chemometry. *Environ. Sci. Nano* **6**, 2641–2651.

Vantelon D., Trcera N., Roy D., Moreno T., Mailly D., Guilet S., Metchalkov E., Delmotte F., Lassalle B., Lagarde P. and Flank A.-M. (2016) The LUCIA beamline at SOLEIL. *J. Synchrotron Radiat.* **23**, 635–640.

Wigginton N. S., Haus K. L. and Hochella Jr M. F. (2007) Aquatic environmental nanoparticles. *J. Environ. Monit.* **9**, 1306.

Wilke M., Farges F., Petit P.-E., Brown G. E. and Martin F. (2001) Oxidation state and coordination of Fe in minerals: An Fe *K*- XANES spectroscopic study. *Am. Mineral.* **86**, 714–730.

Xia X., Wang J., Hu Y., Liu J., Darma A. I., Jin L., Han H., He C. and Yang J. (2022) Molecular Insights into Roles of Dissolved Organic Matter in Cr(III) Immobilization by Coprecipitation with Fe(III) Probed by STXM-Ptychography and XANES Spectroscopy. *Environ. Sci. Technol.* **56**, 2432–2442.

Xu R. K., Hu Y. F., Dynes J. J., Zhao A. Z., Blyth R. I. R., Kozak L. M. and Huang P. M. (2010) Coordination nature of aluminum (oxy)hydroxides formed under the influence of

low molecular weight organic acids and a soil humic acid studied by X-ray absorption spectroscopy. *Geochim. Cosmochim. Acta* **74**, 6422–6435.

Declaration of interests

☒ The authors declare that they have no known competing financial interests or personal relationships that could have appeared to influence the work reported in this paper.

☐The authors declare the following financial interests/personal relationships which may be considered as potential competing interests: